Pergamon

Int. J. Heat Mass Transfer. Vol. 41, No. 2, pp. 335–346, 1998

Printed in Great Britain
0017–9310/98 $19.00+0.00

PII: S0017-9310(97)00148-8

Local convective heat transfer from an array of wall-mounted cubes

E. R. MEINDERS, T. H. VAN DER MEER and K. HANJALIĆ

Delft University of Technology, Faculty of Applied Physics, Lorentzweg 1, PO BOX 5046, 2600 GA Delft, The Netherlands

(*Received* 24 *January* 1997 *and in final form* 1 *May* 1997)

Abstract—The paper presents some results of the experimental investigation of the local convective heat transfer from a wall-mounted *single* array of cubical protrusions along a wall of a wind tunnel. The local convective heat transfer was determined from the surface temperature distribution of the internally heated cubical elements, measured with infrared and liquid crystal thermography, and from the local surface heat flux. In addition, smoke and surface oil-film visualizations were performed to characterize the macroscopic flow-field which provided a basis for a qualitative interpretation of the heat transfer coefficient distributions. The results showed a high non-uniformity of the local convective heat transfer over the surfaces of the individual elements. © 1997 Elsevier Science Ltd.

1. INTRODUCTION

The flow in an electronic cabinet is characterized by the complex interior topology which induces the flow to separate and recirculate locally between the board-mounted electronic components. The thermal analysis of a printed circuit board is made more complicated by the fact that each board-mounted element is a concentrated heat source which causes substantial local buoyancy effects. The heat transfer encountered in this kind of applications is, therefore, usually of a mixed mode involving both natural and forced convection. In addition, a substantial effect may be expected from the radiation, if the temperature of the elements much exceeds that of the surrounding walls. Because of the complex flow pattern, buoyancy and radiation, the convective heat transfer distribution is highly non-uniform, which causes potentially damaging hot spots which may cause malfunction of the circuit board. An accurate prediction of the thermal field on and around the electronic element and the control of critical temperatures of complex cabinet configurations requires a reliable evaluation of local convective heat transfer with a sufficient resolution.

The convective heat transfer distributions in simplified configurations such as two-dimensional ribs mounted on one of the channel walls of a wind tunnel have already been reported in literature. Igarashi and Yamasaki [1] studied the local convective heat transfer from a wall-mounted rectangular block of 10 and 20 mm height and 30 mm depth in a turbulent boundary layer for velocities of the undisturbed flow between 4 and 18 m s^{-1}. They determined the local convective heat transfer coefficient (htc) from a uniform heat flux, supplied by an electrically powered stainless steel sheet, and temperatures measured with thermocouples buried in the material. A large variation in local heat transfer coefficients was observed, in particular at the top face of the rectangular block, which was attributed to the flow separation and reattachment. The heat transfer from an array of multiple wall-mounted ribs in fully developed channel flow was reported by Aliaga *et al.* [2, 3]. They determined the local heat transfer coefficients from a uniform heat flux, generated by an electrically powered metal foil, and the surface temperature distribution, measured with an infrared camera. The Reynolds numbers considered, based on the center-line velocity and hydraulic diameter of the channel, ranged between 0.5×10^6 and 6×10^6. Results for a similar configuration were recently also reported by Lorenz *et al.* [4]. They also used a heated foil and infrared thermography to determine heat transfer coefficients. Reynolds numbers, based on the hydraulic diameter and the mean velocity, ranged from 10^4 to 10^5. Both studies emphasized the difficulties in determining accurately the local heat transfer, and indicated possible causes of temperature inaccuracy when using infrared thermography for the measurement of surface temperature distributions. From these studies it also appeared that flow separation and reattachment dictate to a great extent the local convective heat transfer phenomena. In another paper, Igarashi [5] reported on studies of the local convective heat transfer from a vertical rectangular prism placed in a uniform flow with free stream velocities ranging from 6 to 20 m s^{-1}. The investigation included variation of the width-to-height ratio and the flow Reynolds number. Again, a substantial variation in the convective heat transfer was found. Studies of the heat transfer coefficient distributions of three-dimensional objects are more scarce in the open literature. Natarajan and Chyu [6, 7] researched the local convective mass transfer from a wall-mounted single cube using the naphthalene sublimation technique.

NOMENCLATURE

D	channel width [m]
h, htc	adiabatic heat transfer coefficient [W m^{-2} K^{-1}]
H	cube rib [mm]
i, j, k	indices
L	separation [mm]
n	normal direction
N, M	numbers
Re	Reynolds number $Re = UH/v$
P_{sup}	power supply [W]
Q_{conv}	convective heat flow [W]
Q_{loss}	heat losses [W]
Q_{rad}	radiative heat flow [W]
$T(x, y, z)$	temperature of epoxy substrate [K]
T_{ad}	adiabatic component temperature [K]
T_s	surface temperature [K]
U	bulk velocity [m s^{-1}]
x, y, z	coordinates.

Greek symbols

λ	thermal conductivity [W m^{-1} K^{-1}]
v	kinematic viscosity [m^2 s^{-1}]
ϕ''_{cond}	conductive heat flux at surface [W m^{-2}]
ϕ''_{conv}	convective heat flux [W m^{-2}]
ϕ''_{rad}	radiative heat flux [W m^{-2}].

The cube was placed in a wind tunnel with a flow boundary layer thickness of approximately 1/4 of the cube height. The measurements showed a strong variation in the mass transfer coefficients. Studies of the element-average heat transfer of three-dimensional multiple element configurations are reported by Moffat and Anderson [8–10]. These studies involved the cube average convective heat transfer from aluminum cubes placed in in-line bundles, thus forming a regular matrix. The concept of the adiabatic heat transfer coefficient was successfully applied to describe the convective heat transfer at the element level. Superposition of Kernel functions appeared to be a convenient way to define adiabatic reference temperatures, which incorporate the effect of all upstream thermal boundary conditions. At present, no information can be found in the open literature on the local convective heat transfer at component level for three-dimensional multiple element configurations.

This paper addresses the investigation of the local convective heat transfer from a wall-mounted *single* array of heated cubical protrusions placed in a vertical channel flow. An experimental technique, developed to measure local convective heat fluxes from the surface temperature distribution of the internally heated elements and the local surface heat flux, was used to determine heat transfer coefficients. The surface temperature distributions were acquired from infrared thermography. Both an image restoration technique and an *in situ* calibration procedure were employed to improve the absolute accuracy of the temperatures obtained with the infrared camera. Details about the applied technique and data processing have been reported in ref. [16]. Temperature measurements with a second independent method, liquid crystal thermography, served as validation of the accuracy of the infrared measurements. Flow visualizations were used to elucidate the mean flow structures around the protrusions. The resulting flow-field facilitated the qualitative interpretation of the local convective heat transfer.

2. TEST CONFIGURATION AND PHYSICAL MODEL

The test configuration consisted of a rectangular channel of width $D = 50$ and 500 mm height. A packed array of nine cubical protrusions, size $H = 15$ mm, was placed at half the channel height on one of the vertical walls. The spacing between the cubes was the height of one cube, 15 mm (L = 30 mm). Because of the large height-to-width ratio, the channel flow at the location of the elements was two-dimensional. A schematic of the set-up is given in Fig. 1. The rectangular section was part of the closed wind tunnel with a heat exchanger to thermostat the air to a constant temperature of 21.0°C. Honeycombs and grids were used to filter out the large turbulence scales. A laminar boundary layer flow developed along the test-section walls. This resulted in a boundary layer thickness of approximately half a cube in height at the location of the array. The measurements were performed at some values of the Reynolds numbers, 795, 2086, 3278 and 5066, based on the bulk velocity and cube height.

The first six protrusions (E1–E6) in the packed array were used to determine local convective heat transfer coefficients. Two additional cubes enabled the *in situ* calibration (element 7) and the location identification of the obstacles (element 9). Cube 8 was used to establish an appropriate environment for the *in situ* calibration. This nomenclature is used in the sketch in Fig. 1.

The cubes are made of an internal copper cubical core of 12.5 mm in size with an epoxy mantle of 1.5 mm thickness (see Fig. 1 and ref. [16]). Controlled powering of the element with a heat source embedded in the copper core resulted in an almost uniform cop-

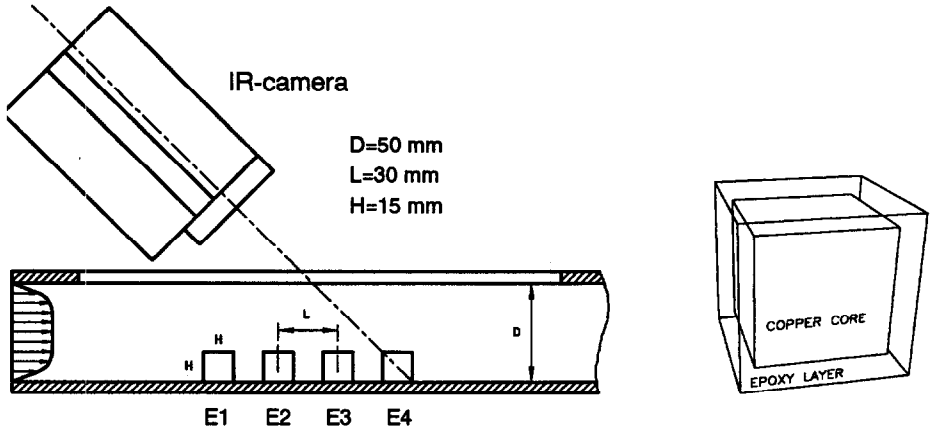

Fig. 1. Schematic sketch of the test configuration and the composed measurement element.

per temperature with the tolerance of 0.05°C, as a result of the high thermal conductivity of copper, in contrast to that of the epoxy substrate. All experiments presented in this paper were performed at a copper core temperature of 75.0°C. The uniform copper temperature provides the temperature boundary condition for the inner bound of the epoxy layer. The surface temperature distribution of the outer bound of the substrate, acquired from thermography experiments, provides the outer boundary condition. A simple one-dimensional analysis which ignores the lateral conductive heat fluxes, especially close to the edges, resulted in an unacceptably high error. Therefore, the temperature distribution in the epoxy substrate was calculated numerically by solving the equation for the three-dimensional conduction problem:

$$\frac{\partial}{\partial x_i}\left(\lambda_{i,j}\frac{\partial T}{\partial x_j}\right) = 0 \tag{1}$$

where $T(x, y, z)$ is the temperature distribution and $\lambda_{i,j}$ is the anisotropic thermal conductivity. Measurements showed an isotropic thermal conductivity of 0.24 W $(\mathrm{mK})^{-1}$ independent of direction and temperature so that equation (1) reduces to the ordinary Laplace equation. Once the temperature distribution in the epoxy layer is known, the spatial temperature gradient in normal direction at the surface can be calculated thus yielding the local conductive heat flux:

$$\phi''_{\mathrm{cond}}|_s = -\lambda\frac{\partial T}{\partial n} \tag{2}$$

where n is the direction normal to the surface. The local net radiative heat flux was calculated from the surface temperature distribution, ambient temperatures (channel walls), surface emissivity and view factors. A heat balance at the surface yields the local convective heat flux ϕ''_{conv}, and thus the local heat transfer coefficient:

$$h = \frac{\phi''_{\mathrm{cond}}|_s - \phi''_{\mathrm{rad}}}{T_s - T_{\mathrm{ad}}} \tag{3}$$

where ϕ''_{cond} and ϕ''_{rad} are the conductive and radiative heat flux. T_s and T_{ad} denote the surface and the adiabatic temperature respectively. The latter is defined as the surface temperature of an element in the adiabatic situation. The adiabatic temperature was measured in a separate experiment in which only the cube under consideration was cut from the power supply while all other elements remained operational. The surface temperature of the unpowered element approaches the copper core temperature since the temperature decay across the epoxy layer was negligible within the tolerance of the experimental uncertainty. The unpowered temperature approaches the adiabatic temperature in the case of negligible heat losses [8]. The convective heat transfer results obtained with this technique are not influenced by the heat losses through the mounting base and lead wires.

3. THERMOGRAPHY

An infrared imaging system was used to acquire the surface temperature distributions of the five faces of an element exposed to air flow. Infrared surface temperature measurements of small objects is hampered by significant spatial image degradation which becomes a limiting factor in accurate surface temperature analysis, in particular when a large spatial resolution and depth-of-field are required [12, 13]. The degradation, as encountered in the present study, was corrected for by restoration of the infrared images with a Wiener filter. This restoration technique is based on the measured two-dimensional optical transfer function which is a characteristic of the infrared imaging system used. Specifications of the infrared camera and details of the restoration technique are given in refs. [14] and [15].

The lateral side faces of the cubes, which are orientated perpendicular to the mounting base, were scanned under a 45° scan angle because of the geometrical restrictions of the closed wind tunnel. This scan facility is also drawn in Fig. 1. In order to enhance the thermal radiation, the surface of the cube was coated with a high emissivity paint with an emissivity

of 0.95. For scan angles up to approximately 55–60°, the emissivity appeared to be independent of the scan angle. The depth-of-field of the infrared camera was sufficiently large (±5 mm) to enable accurate measurement of the surface temperature across the entire angled faces. The faces were divided in 900 surface grid cells for which the average pixel value was calculated. The sensor exposed to radiation receives an intensity which consists of various environmental contributions, among others, emission from the object, reflections from hot neighboring elements, reflections from the channel walls, attenuation by the wind tunnel foil, reflections on this foil, etc. [11]. Since these contributions are difficult to quantify individually, an *in situ* calibration was employed which provides the relation between the camera intensity and the surface temperature. The measurement element was replaced by a pure copper element from which the surface temperature can easily be measured. The dimensions and surface emissivity of the calibration element were similar to those of the measurement elements. Its high thermal conductivity resulted in a uniform internal and surface temperature (tolerances were within 0.05°C), which was measured with a thermocouple embedded in the cube. Variation of the supplied power, and thus cube temperature, finally resulted in calibration curves describing the relation between the infrared camera output and the surface temperature for each location at the cube surface. The infrared technique, including the mapping and *in situ* calibration, involved a spatial accuracy of 0.5 mm.

Liquid crystal thermography was used as a second independent measurement technique to provide validation of the accuracy of the infrared surface temperature measurements. Thermochromic liquid crystals, having both the properties of a liquid and crystalline state, provide a relation between color and temperature. Details of the properties and applications of thermochromic liquid crystals can be found in refs. [17] and [18]. In this study, a mixture of five liquid crystals was used, which resulted in five temperature events. The selected crystals had a narrow color-play bandwidth of approximately 2°C and event temperatures around 47, 55, 60, 65 and 73°C. Two calibration methods were used to obtain an objective temperature reading at the very sharp color change from green to red. The first method was, in principle, based on an *a priori* known temperature distribution of a heated surface which was brushed with the same liquid crystal mixture. In the other method, a pure copper element was used which was controlled at a constant temperature within a tolerance of 0.05°C. Care was taken to guarantee similar experimental conditions during the calibration when employing each of the methods, such as source and angle of illumination, age of mixture, etc. [16]. The resulting temperatures at the sharp green-to-red transitions are 47.5, 55.8, 60.5, 65.2 and 72.8°C, accurate within 0.4°C. This accuracy was estimated from an uncertainty analysis. The liquid crystal technique incorporates a spatial accuracy of approximately 0.5 mm. A disadvantage of this approach of considering only color transitions between green and red is the poor spatial resolution. Advantages are the objectivity and the good overall accuracy of the acquired temperatures, which make this method an excellent back-up for validation of the infrared and other techniques.

4. ACCURACY OF EXPERIMENTAL RESULTS

The accuracy of the experimental results was evaluated with an uncertainty analysis as recommended by Moffat [19]. The uncertainty in the various quantities measured is reflected in the overall accuracy of the heat transfer coefficient. Some major contributions are addressed in this paper, but a more detailed analysis is given in ref. [16]. The epoxy layer was carefully machined with deviations in thickness of approximately 0.01 mm. The effect of thermal expansion gave a relative increase in thickness of less than 0.6%. The thermal conductivity λ was determined experimentally and yielded a value of 0.24 $W\,m^{-1}\,K^{-1}$ with an accuracy of 2%. The real conductive heat flux is related to the internal epoxy substrate temperature, which is the numerical solution of the Laplace equation with the surface temperatures as boundary conditions. The truncation error appeared to be negligible and, therefore, the uncertainty in the calculated substrate temperature is of the same order of magnitude as the uncertainty in the copper and surface temperature. The copper temperature, measured with an embedded and calibrated thermocouple, yielded an accuracy of 0.1°C. The emissivity of the black paint, measured within an accuracy of 2%, was 0.95. The ambient and adiabatic reference temperatures are accurate within 0.5°C; these temperatures make minor contributions to the total error in the heat transfer coefficient. The surface temperature has a large impact on the overall accuracy. Application of both the *in situ* calibration and image restoration technique resulted in an absolute accuracy of 0.4°C in the infrared surface temperatures. Both thermography techniques incorporate a spatial accuracy of at least 0.5 mm. Close to the edges, the temperature reading is less accurate, approximately 0.6°C, because of the effects of image mapping. The accumulation of errors finally results in approximately 5–10% inaccuracy in the local heat transfer coefficient [16], the higher values pertaining more to the edge areas.

5. RESULTS

5.1. *Surface temperature measurements*

To enable the validation of the infrared temperature measurements with the results from the liquid crystal technique, well-controlled experimental conditions are guaranteed during both surface temperature measurements. These conditions include power supply, air temperature, air flow, etc. Liquid crystal and infrared temperature measurements are presented

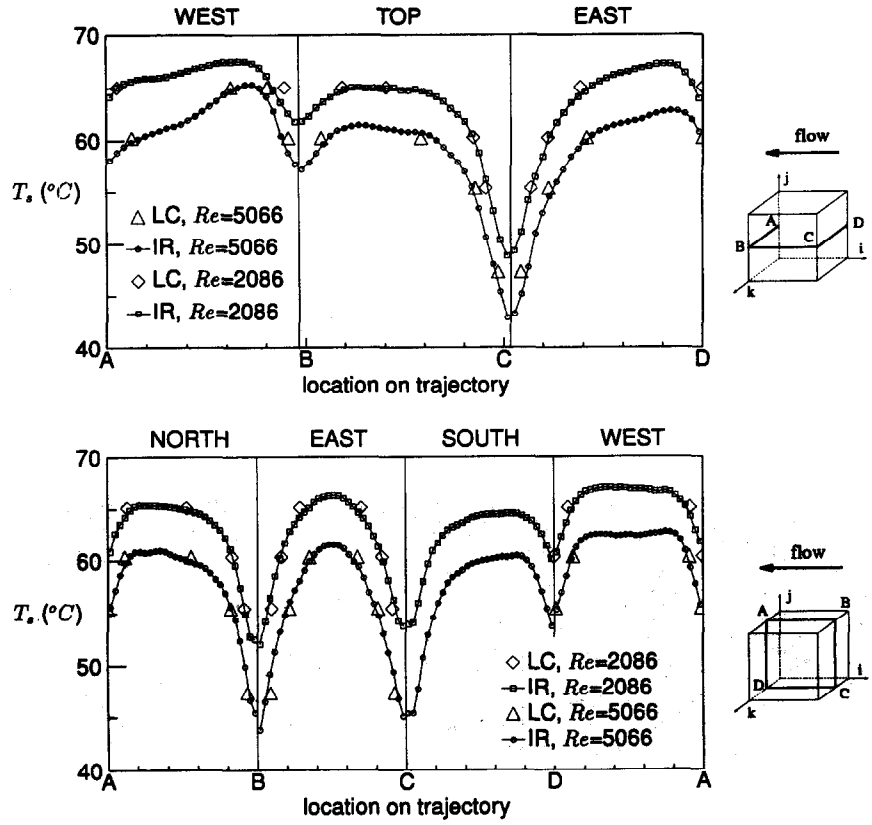

Fig. 2. Surface temperatures along trajectory I (upper plot) and trajectory II (lower plot) on the fifth element for $Re = 2086$ and 5066: comparison of liquid crystal measurements (LC, ◇ and △) and infrared thermography (IR, □ and ○).

in Fig. 2. The results for the fifth element along trajectories I and II are shown. Trajectory II denotes the cross-section of a plane at half cube height, parallel to the mounting plate; trajectory I is the cross-section of the plane at the center line of the array oriented perpendicular to the base plate. The liquid crystal measurements, (isotherms at the surface and, therefore, only available at certain temperature levels), are indicated by symbols (△) and (◇) for $Re = 2086$ and 5066, respectively. Infrared temperature measurements, based on images which were processed with the restoration filter and *in situ* calibration, are indicated as lines with symbols (□) and (○) for the same Reynolds numbers. The temperatures of both methods coincide within the experimental uncertainty of the LC measurements. This confirms the necessity of the applied image restoration and, further, it provides an accuracy estimate of 0.4°C for the infrared temperatures. The small deviations between each of the techniques are attributed to experimental uncertainty in both the spatial and temperature readings.

Isotherm maps of the five faces exposed to air flow for the first six subsequent protrusions in the packed array are given in Fig. 3. The cube faces are folded out and projected in one plane. The upper and lower plots correspond to $Re = 5066$ and 795, respectively. It is important to note that the isotherm maps for $Re = 5066$ are all symmetric, which points at a forced convection situation. The surface temperature distribution of the first element for $Re = 795$ is also symmetric; however, the pronounced temperature gradients in the vertical direction are observed for the down-stream elements, especially for the front and rear face. These gradients indicate vertical fluid motion caused by the thermally driven natural convection. The large spatial gradients in surface temperature at the individual elements, as well as the differences between subsequent cubes, indicate a significant variation in the convective heat transfer coefficients. A more detailed discussion is given below.

5.2. *Macroscopic flow features*

The flow-field around the array of cubes was deduced from smoke and oil-surface visualizations. Smoke visualizations were performed with smoke injection and laser sheet illumination in planes parallel and perpendicular to the channel wall. An instantaneous smoke visualization at the symmetry plane $y/H = 0$ is given in Fig. 4, it shows the first three elements in the single array. A typical oil-surface visualization of the mean surface flow patterns around the protrusions is shown in Fig. 5. The surface streak lines in the oil pattern are parallel to the flow direction and are therefore referred as surface stream lines.

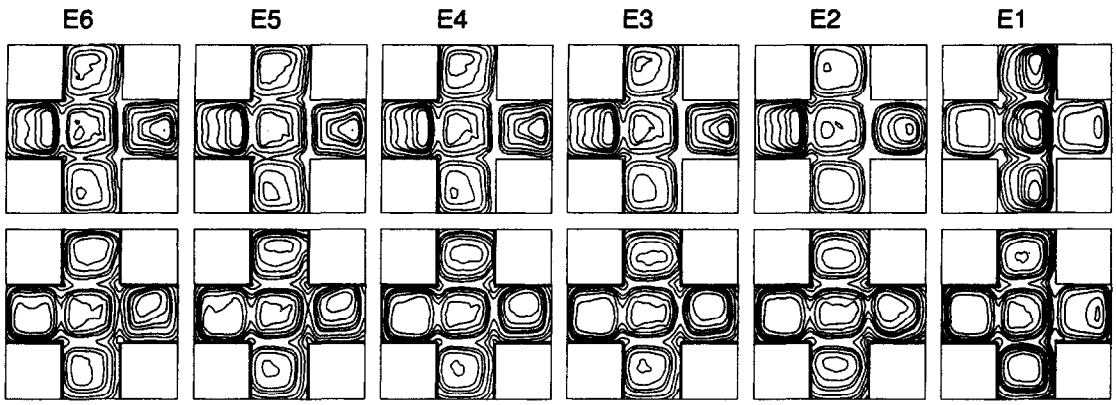

Fig. 3. Infrared surface temperature maps of elements E1–E6 for $Re = 5066$ (first series) and $Re = 795$ (second series).

Fig. 4. Smoke visualization of the flow patterns around the single array of cubical protrusions at the symmetry plane $y/H = 0$.

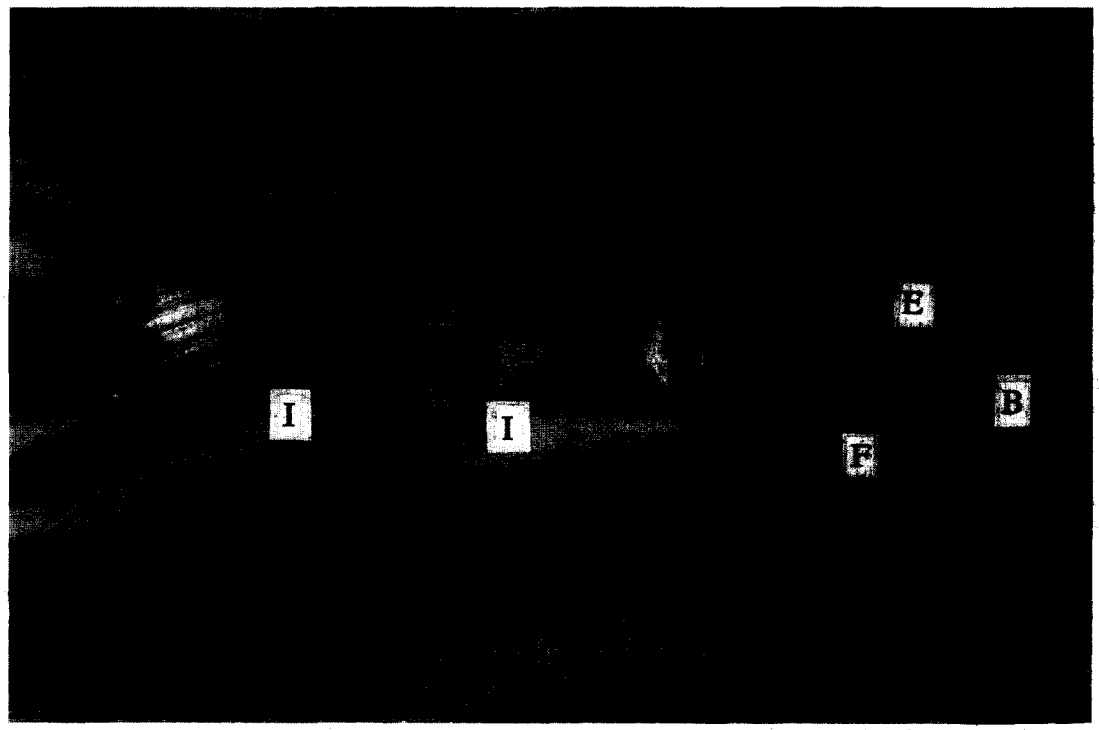

Fig. 5. Oil-surface visualizations around the single array of cubical protrusions.

Accumulations of the visualization fluid indicate lines of flow separation and, conversely, lines of flow (re)attachment appear as areas of dilute visualization pigment. The mean flow patterns are deduced from a topological analysis. A more detailed description of this visualization technique can be found in ref. [20]. For both visualizations, the flow direction was from right to left. A three-dimensional sketch of the flow

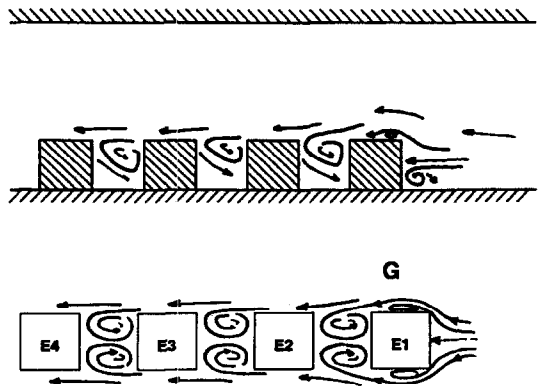

Fig. 6. Schematics of the cross-sections of the flow patterns. Upper plot: xz-plane at center line $y/H = 0$ and lower plot: xy-plane at half cube height $z/H = 0.5$.

field around the first four protrusions in the packed array is given in Fig. 7. Cross-sections of this sketch at the symmetry plane $y/H = 0$ and a plane parallel to the channel wall at $z/H = 0.5$ are shown in Fig. 6(a, b), the upper and lower plot, respectively. It is important to note that the sketched flow-field is valid for the three largest Reynolds numbers studied. For $Re = 795$, the flow-field deviates because of the buoyancy induced flow motion.

The flow-field in the proximity of the leading cube is characterized by a horseshoe vortex structure, marked with **A** in Fig. 7, induced at the windward face and extending along both lateral sides of the array in the downstream direction. A cross-section of this vortex structure upstream of the leading cube at $y/H = 0$ can clearly be observed in Fig. 4. The pigment pattern given in Fig. 5 shows its footprint at the channel wall. The center of the main horseshoe vortex, indicated by the bent white band, is marked with **B**. Besides the main vortex, a secondary vortex is found upwind, marked with **C** in Fig. 7. The flow in the proximity of the horseshoe vortex is unsteady in nature, thus giving rise to bimodal velocity distributions. This unsteadiness was clearly observed from the recorded smoke visualizations. A bounded vortex, indicated by **D**, is found at the top face of the leading element. The footprint of this vortex on the top face appears as the two counter-rotating circles which can be observed from the oil-surface image (marked with **E**). A strong recirculation is also prevalent at the lateral side faces, see **F** in Fig. 7. These vortex tubes cover a substantial part of the surface. Their footprints on the channel

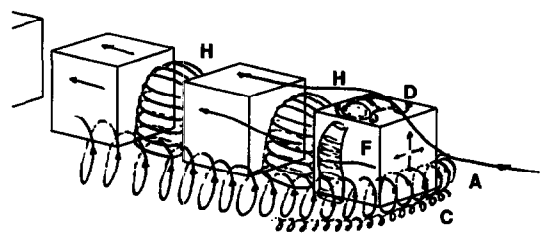

Fig. 7. Three-dimensional sketch of the mean flow-field.

wall can be observed in the oil–graphite image, marked with **F**. The flow sketch at $z/H = 0.5$, given in Fig. 6(b), shows the cross-section of this vortex tube (**G**). The smoke visualization recordings on video tape, despite difficulties in identifying the pattern in single instantaneous images, confirmed on the whole these flow recirculations. The extensions of the horseshoe vortex reattach at the side faces of the second tube. The shear layer over the top face of the first cube reattaches also at the second cube. For the second and subsequent cubes, shear flow is found at these faces with the absence of flow reversal. Strong arch-shaped vortices, confined by the main flow, exist in the gaps between subsequent cubes. Figure 7 clearly shows these vortices, marked with **H**. Their two strong counter-rotating extensions appear from the nodes marked with **I** in Fig. 5. Cross-sections of these structures at the planes $y/H = 0$ and $z/H = 0.5$ are given in Fig. 6(a, b), respectively. Besides the somewhat broader arch vortex between the leading and the second cube, compared to the one further downstream, no significant differences in the flow-field appear after the second element. The flow-field around the leading cube shows remarkable similarities with the flow around a single wall-mounted cube in a fully-developed channel flow, as studied by Martinuzzi [20]. He also found the horseshoe vortex, flow recirculations at the side and the top faces and the arch vortex characterizing the macroscopic flow field around the single cube.

5.3. *Local convective heat transfer*

The heat transfer coefficient distribution along trajectory II is given in Fig. 8 as a function of the six element positions and parametric in the Reynolds number. Local heat transfer coefficients along trajectory I are given in Fig. 9. The uppermost plot corresponds to the leading element, the lowest plot to the sixth element. Buoyancy effects, induced by the temperature difference between the heated elements and the surrounding air, are of negligible importance for the three largest Reynolds numbers studied. Symmetric profiles are found for these situations on the north (A–B) and south (C–D) face for all elements. The local heat transfer phenomena at the lateral and top faces of the leading element are dominated by the flow recirculations which are most prevalent for the largest Reynolds number. The separation of the vortex tube at the side faces, found in the proximity of the leading edge, causes a minimum of the convective heat transfer. Increased convective heat transfer is found downstream near the trailing edge where the main flow attaches. This heat transfer coefficient distribution was also observed by Igarashi and Yamasaki [1] at the top face of a single wall-mounted rectangular rib in a turbulent boundary layer flow. Impinging heat transfer occurs at the front face (east, B–C), facing the cold oncoming flow, thus leading to the highest convective heat transfer. Close to the channel wall,

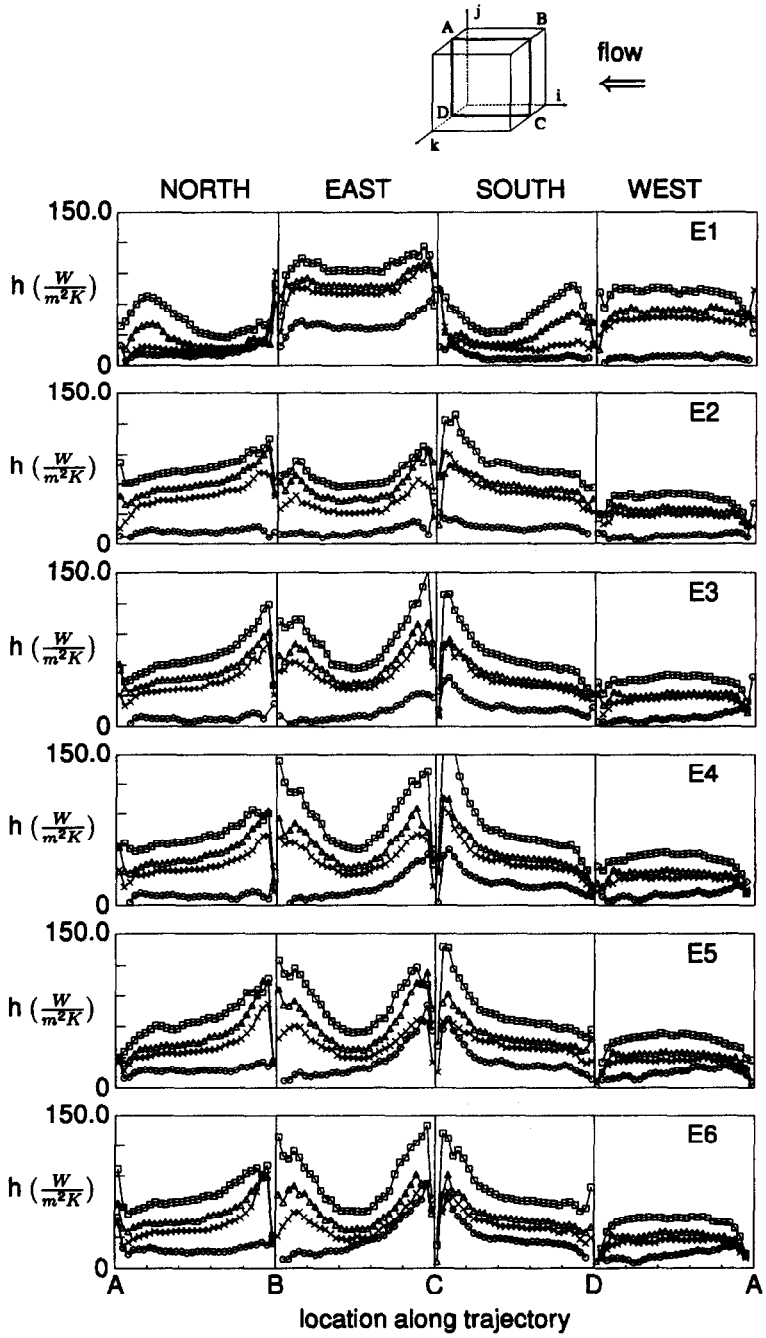

Fig. 8. Heat transfer coefficients for cross-section II for elements E1–E6 parametric in Reynolds number: ○ $Re = 795$, × $Re = 2086$, △ $Re = 3278$ and □ $Re = 5066$.

the local minimum at this front face can be explained by the rotating horseshoe vortex (see Fig. 9).

The convective heat transfer from the lateral and top faces of the second element, governed by the attached boundary layer flow, is characterized by a strong decay in the direction of the rear edge. The relatively high heat transfer coefficients are caused by the reattaching horseshoe vortex and main flow. The concave profiles in the heat transfer coefficients at the east (front) face are explained by the counter-rotating extensions of the arch-shaped vortex which envelopes the gap between the leading and the second element. The heat transfer at the rear face is uniform at the cross-section at $z/H = 0.5$, however, a local minimum, accompanied by a small local maximum, is found at the upper edge. These local extrema are caused by the rotating arch-shaped vortex. The convective heat transfer at the lateral side faces for the subsequent elements is dictated by boundary layer flow. Along the surface, the heat transfer decays in the downstream direction. Aliaga *et al.* [2, 3] observed similar behavior at the top face of multiple wall-mounted ribs in a fully

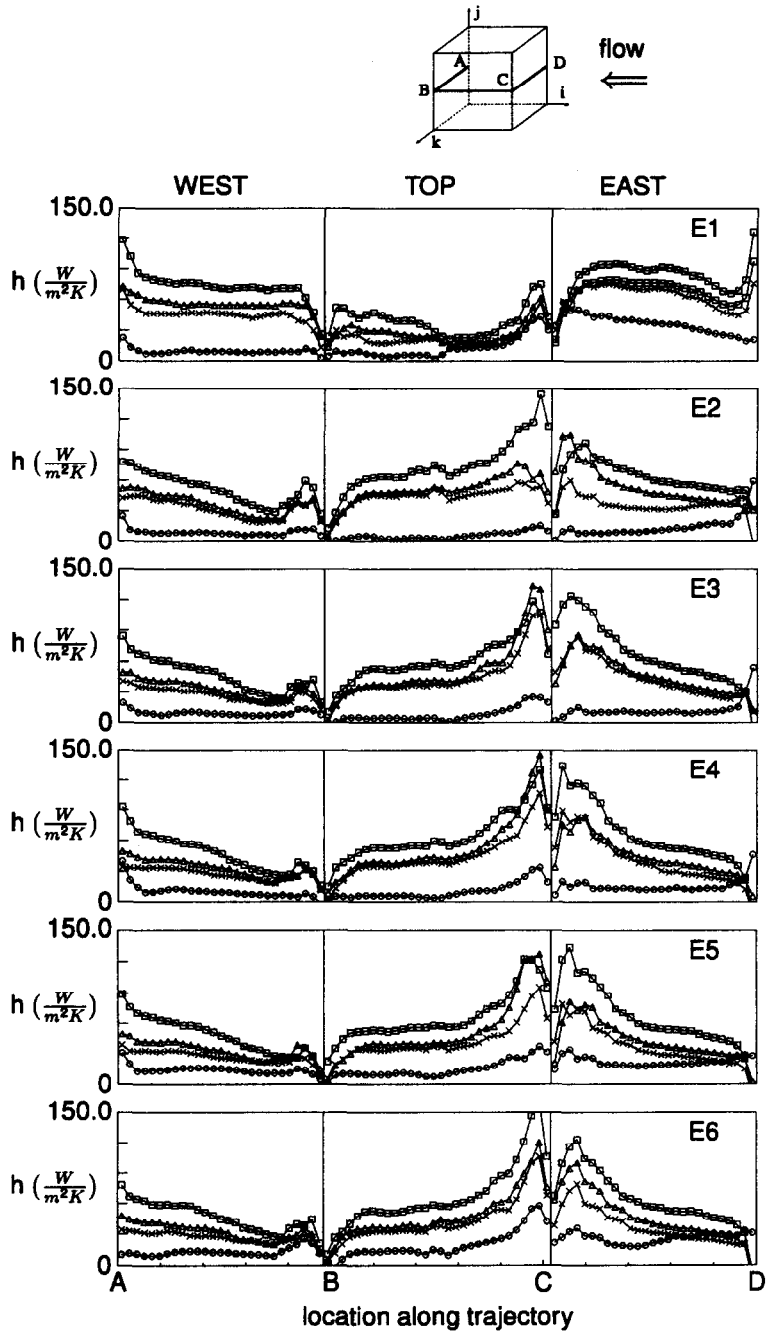

Fig. 9. Heat transfer coefficients for cross-section I for elements E1–E6 parametric in Reynolds number: ○ $Re = 795$, × $Re = 2086$, △ $Re = 3278$ and □ $Re = 5066$.

developed channel flow. The heat transfer at the front face is still characterized by concave profiles, caused by the arch vortex. The local extrema at the rear face also remain. No significant differences are observed downstream of the third protrusion.

Significant buoyancy effects appear for $Re = 795$, which classifies the situation as mixed convection. The temperature-driven buoyancy flow is relatively strong in the gaps between the subsequent elements. The arch-shaped vortex, which was found for the forced convection dominated flow situations (the three largest Reynolds numbers studied), breaks up because of the induced flow motion directed perpendicular to the main flow. The resulting flow pattern causes an increase in the heat transfer at the south-front-edge, decaying in the downstream direction along C–D (south face) and the negative gravity direction along C–B (back face), see Fig. 8. The opposite behavior occurs at the opposing face, although the effects are weaker. This can also be seen in Fig. 8. These buoyancy effects become more pronounced for the downstream protrusions. The induced buoyancy flow

appears also from the isotherm plots, shown in Fig. 3 in the lower series. Differences in temperature gradients indicate the stream direction of the flow.

5.4. *Averaged convective heat transfer*

Surface averaged heat transfer coefficients were derived from the ratio of the surface-integrated convective heat flux and the difference between the averaged surface temperature and references temperature:

$$\bar{h}_{ad} = \frac{\frac{1}{M}\sum_{i,j} q_{conv}}{\frac{1}{M}\sum_{i,j} T_s - T_{ad}} \quad (4)$$

where i and j are the indices denoting the location at the surface and M is the total number of surface cells per face. The surface averaged heat transfer coefficients for the five separate faces are shown in Fig. 10 as a function of the element location and parametric in the Reynolds number. As is usually the case, the largest Reynolds number causes the largest average convective heat transfer coefficients and vice versa. The oncoming flow impinges at the front face of the leading cube and, hence, results in a large heat transfer coefficient. The front of the second cube is exposed to the arch-shaped vortex. This vortex is continuously supplied with cold air from the horseshoe vortex and the main stream with the consequence of relatively high cooling rates. This also applies to the subsequent element downstream in the array. The convective heat transfer at the rear face of the first element is relatively high because of the prevalent arch-shaped vortex between the first two elements. The heat transfer at the rear faces of the second and third protrusion is much smaller, which is explained by the decreasing impact of the bounded vortices further downstream. The strong flow reversals at the lateral faces of the first cube cause a notable minimum in the convective heat transfer. In contrast, the second element is exposed to the reattached flow from the horseshoe vortex and main stream and, therefore, its convective heat transfer rate is significantly higher. This feature appears at the three highest Reynolds numbers. The impact of the horseshoe vortex diminishes for the downstream elements, which results from the lower heat transfer rate for the third element. A bounded vortex system envelopes the top face of the leading element, as a consequence of the separating main stream, thus resulting in a significantly lower convective heat flux. The flow attaches at the top of the second element and causes a high convective heat transfer rate at this face.

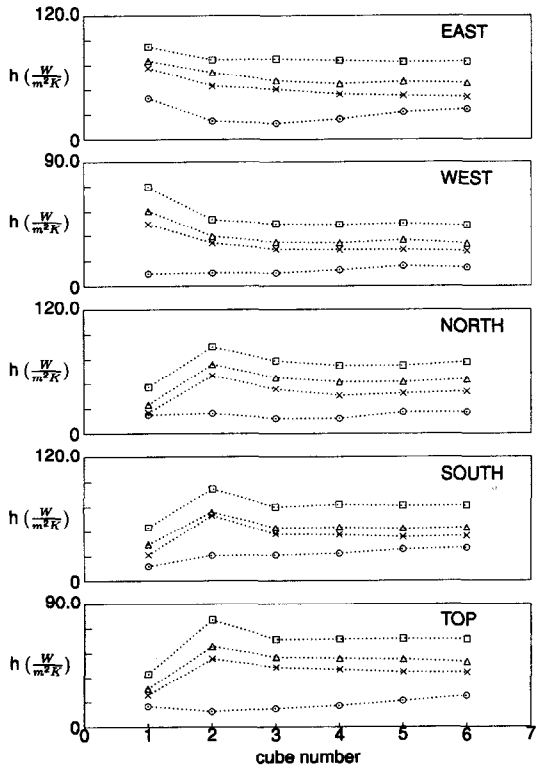

Fig. 10. Surface averaged htcs, parametric in element location: ○ $Re = 795$, × $Re = 2086$, △ $Re = 3278$ and □ $Re = 5066$ for the east, west, north, south and top face.

Substantial variation in the averaged heat transfer coefficients is found for the first three protrusions in the array. After the third element, the flow becomes gradually fully developed and no notable variation in the convective heat transfer is observed. This is the consequence of using the concept of the adiabatic heat transfer coefficient. The small deviations for the remaining elements, as appear from the plots, are attributed to the experimental uncertainty.

The average convective heat transfer for the mixed convection case, $Re = 2086$, differs somewhat from the others. In particular, for the cubes further downstream in the array, the heat transfer benefits from the buoyancy-induced vertical fluid motion, which results in an enhancement of the heat transfer coefficient.

The heat transfer coefficients averaged over all five cube faces are given in Fig. 11 as functions of the element location. Even at the cube level, the recirculative flow-field around the leading cube dictates a pronounced minimum. The second element shows a maximum in the heat transfer coefficient because of the interaction with the horseshoe vortex and main flow. Anderson and Moffat [10] performed cube-average heat transfer experiments for a regular matrix of wall-mounted aluminum cubes in a channel flow. The spacing between the cubes was 2 cube widths, i.e. $L/H = 3$. The results of their study are also plotted in Fig. 11 for $Re = 2980$ and 6656 at a channel width to cube ratio of $D/H = 4.6$. Although a somewhat different geometry was studied, their results are in good agreement with the present findings. They also found that the convective heat transfer is minimum for the leading element and maximum for the second cube. Figure 12 gives the Reynolds number dependence on the heat transfer coefficient in log coordinates. The cube-average heat transfer coefficients vs

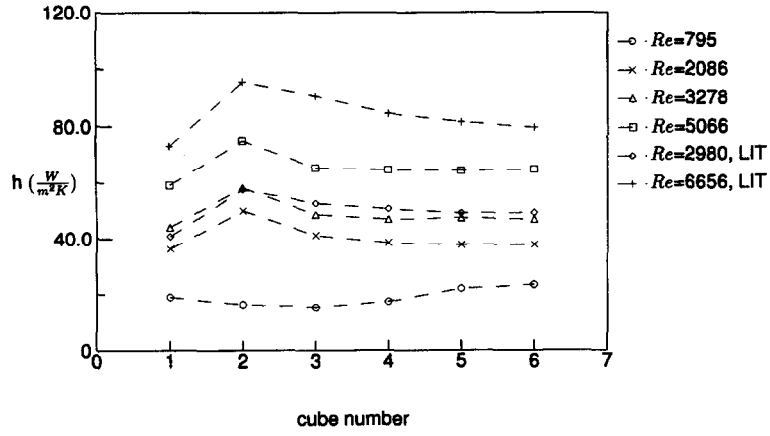

Fig. 11. Cube averaged htcs, parametric in element location: ○ $Re = 795$, × $Re = 2086$, △ $Re = 3278$ and □ $Re = 5066$. Literature data (LIT): ◇ $Re = 2980$ and + $Re = 6656$ [10].

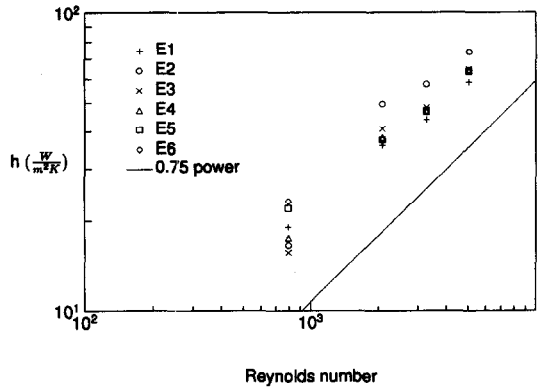

Fig. 12. Cube averaged htcs as function of the Reynolds number based on the channel width: + E1, ○ E2, × E3, △ E4, □ E5 and ◇ E6.

the Reynolds number, based on the cube height and bulk velocity, parametric in the element location are shown. The correlation $Nu \propto Re^{0.75}$, which usually represents forced convective heat transfer problems, seems to be applicable only to the two largest Reynolds numbers studied.

5.5. *Integral analysis*

An integral analysis was conducted to estimate the conductive heat losses through the interface of channel wall and cube and through the lead wires. The difference between the supplied power P_{sup} and the sum of total convection Q_{conv} and radiation Q_{rad} defines the total heat losses Q_{loss}:

$$Q_{lcss} = P_{sup} - Q_{conv} - Q_{rad}. \quad (5)$$

The term $Q_{conv} + Q_{rad}$ defines the total conductive heat flow through the five faces of the cube exposed to air flow as calculated from the conduction analysis. The supplied power, determined from the measured voltage and current, is depicted in Fig. 13. The power supply to the second element is maximum for the three largest cooling rates, which confirms the observations made above. Since the main stream is preheated by upstream elements, a continuous decrease in the supplied power is encountered in the downstream direction. The power supply for $Re = 795$ differs from that of the other cases. It is maximum for the leading element and, after a decrease in the downstream direction, a slight decrease is observed. The power supply for $Re = 1589$ is added to illustrate the transition regime between $Re = 795$ and 2086. For this cooling rate also, the power supply was slightly larger for the second element, but the transition is obvious. The heat losses in terms of percentage of the power supply range between approximately 25% for $Re = 795$ and 10% for $Re = 5066$.

6. CONCLUSIONS

The experimental investigation of the convective heat transfer distributions of a packed array of wall-mounted cubical protrusions in vertical channel flow leads to the following conclusions:

- The complex vortex structure of the flow-field around the individual elements causes a large non-uniformity in the convective heat transfer distributions. In particular, the flow separation and reattachment at the top and side faces of the first cube and the strong arch-shaped vortices between subsequent cubes give rise to significant differences in the heat transfer coefficients. It is shown that regions of intense flow separation are usually associated with a poor convective heat transfer and, in contrast, regions with flow reattachment exhibited the opposite.
- A substantial variation in average convective heat transfer is found along the array of cubes, in particular for the first three subsequent protrusions. The leading cube appeared to have the lowest aver-

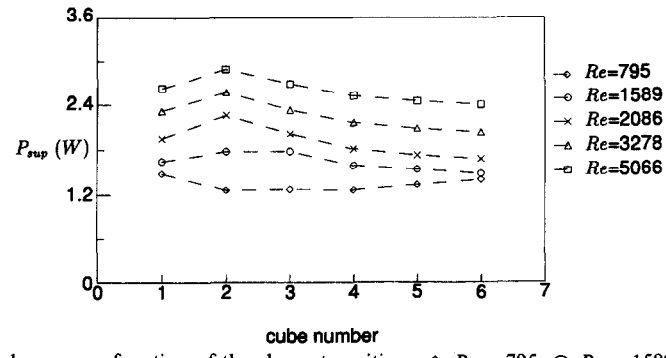

Fig. 13. Supplied power as function of the element position: ◇ Re = 795, ○ Re = 1589, × Re = 2086, △ Re = 3278 and □ Re = 5066.

age convective heat transfer for the three largest Reynolds numbers studied. This is the consequence of the strong vortices at both the lateral and the top faces. The second element, however, is situated in the wake of the first element and experiences a direct interaction with the horseshoe vortex and the separated shear layer which flows over the top of the leading cube. Fully developed heat transfer is found starting from the third element.

- Buoyancy effects impose a significant effect on the convective heat transfer for the lowest Reynolds number studied, Re = 795. Especially in the gaps between subsequent elements, vertical fluid motion causes an asymmetric heat transfer distribution.
- The accuracy of the infrared surface temperature measurements of small three-dimensional wall-mounted cubes was enhanced by the application of an *in situ* calibration and an image-restoration technique. Surface temperatures acquired from liquid crystal thermography, estimated to be accurate within 0.4°C, confirmed the improvements gained from both techniques.

Acknowledgements—This work was funded by Philips Research, Philips, the Netherlands. Thanks are due to Jaap Beekman and Bart Hoek for their technical assistance.

REFERENCES

1. Igarashi, T. and Yamasaki, H., Fluid flow and heat transfer of a two-dimensional rectangular block in the turbulent boundary layer on a plate. *Proceedings, ASME/JSME Thermal Engineering Joint Conference*, 1991, Book no. 10309B, pp. 341–347.
2. Aliaga, D. A., Lamb, J. P. and Klein, D. E., Convective heat transfer distributions over plates with square ribs from infrared thermography measurements. *International Journal of Heat and Mass Transfer*, 1994, **37**(3), 363–374.
3. Aliaga, D. A., Klein, D. E. and Lamb, J. P., Heat transfer measurements on a ribbed surface at constant heat flux using infrared thermography. *Experimental Heat Transfer*, 1993, **6**, 17–34.
4. Lorenz, S., Mukomilow, D. and Leiner, W., Distribution of the heat transfer coefficient in a channel with periodic transverse grooves. *Experimental Thermal and Fluid Science*, 1995, **11**, 234–242.
5. Igarashi, T., Local heat transfer from a square prism to an air stream. *International Journal of Heat and Mass Transfer*, 1986, **29**(5), 777–784.
6. Natarajan, V. and Chyu, M. K., Effect of flow angle-of-attack on the local heat/mass transfer from a wall-mounted cube. *Journal of Heat Transfer*, 1994, **116**, 552–560.
7. Chyu, M. K. and Natarajan, V., Local heat/mass transfer distribution on the surface of a wall-mounted cube. *Journal of Heat Transfer*, 1991, **116**, 552–560.
8. Moffat, R. J. and Anderson, A. M., Applying heat transfer coefficient data to electronics cooling. *Journal of Heat Transfer*, 1990, **112**, 882–890.
9. Anderson, A. M. and Moffat, R. J., The adiabatic heat transfer coefficient and the superposition kernel function: part I—data for arrays of flatpacks for different flow conditions. *Journal of Electronic Packaging*, 1990, **114**, 14–21.
10. Anderson, A. M. and Moffat, R. J., Convective heat transfer from arrays of modules with non-uniform heating: experiments and models. Ph.D. thesis, Report no. HMT-43, 1990.
11. Modest, M. F., *Radiative Heat Transfer*, International editions. McGraw-Hill, New York, 1993.
12. Bougeard, D., Vermeulen, J. P. and Baudoin, B., Mesure du champ de temperature sur une ailette d'echangeur par thermographie infrarouge. *Revue Generale de Thermique*, 1995, **34**(400–401), 325–334.
13. Mullikin, J. C., Vliet, L. J. van, Netten, H., Boddeke, F. R., Feltz, G. van der and Young, I. T., Methods for CCD camera characterization. *SPIE—The International Society for Optical Engineering*, 1994, **2173**, 73–84.
14. Varioscan, *Handbook*. Jenoptik Technology, Jena, Germany, 1990.
15. Meinders, E. R., Kempen, G. M. P. van, Vliet, L. J. van and Meer, T. H. van der, Accurate infrared surface temperature measurements of small cubes using image restoration and *in situ* calibration, submitted for publication consideration, 1997.
16. Meinders, E. R., Meer, T. H. van der, Hanjalić, K. and Lasance, C. J. M., Application of infrared thermography to the evaluation of local convective heat transfer on arrays of cubical protrusions. *International Journal of Heat and Fluid Flow*, 1996, **18**(1), 152–159.
17. Moffat, R. J., Experimental heat transfer. *Proceedings of the 9th International Heat Transfer Conference*, Jerusalem, Israel, Vol. 1, 1990, pp. 187–205.
18. Baughn, J. W., Liquid crystal methods for studying turbulent heat transfer. *Proceedings, International Symposium on Turbulence, Heat and Mass Transfer*, Lisbon, Portugal, 1994.
19. Moffat, R. J., Describing the uncertainties in experimental results. *Experimental Thermal and Fluid Science*, 1988, **1**(1), 3–17.
20. Martinuzzi, R., Experimentelle Untersuchung der Umstroming wandgebundener, rechteckiger, prismatischer Hindernisse. Ph.D. thesis, Erlangen, Germany, 1992.